Chapter 8
Remote Sensing Applications in Satellite Oceanography

Giuseppe Aulicino, Yuri Cotroneo, Paola de Ruggiero, Andrea Buono, Valeria Corcione, Ferdinando Nunziata, and Giannetta Fusco

Contents

Abstract Satellite remote sensing provides repeated global observations of key ocean surface variables. These observations are complementary to in situ measurements. In fact, remotely sensed information fills some in situ gaps in temporal and spatial coverage, while in situ measurements, being a point-wise source of information, provide critical ground-truth for satellite retrievals calibration and validation. Advances in satellite ocean technology and algorithm research make satellite remote sensing an indispensable tool for environmental monitoring of the open and coastal ocean. Moreover, remotely sensed products support the interpretation and the prediction of oceanic phenomena that occur at regional and mesoscales in a synoptic way. In this chapter, we introduce basics of satellite oceanography, including the most used satellite orbits, the range of frequencies involved, and the processing levels related to the remote sensed products. Then, selected ocean products and their

G. Aulicino (✉) · Y. Cotroneo · P. de Ruggiero · G. Fusco
Department of Science and Technology, University of Naples "Parthenope", Centro Direzionale, Isola C4, Naples, Italy
e-mail: giuseppe.aulicino@uniparthenope.it; yuri.cotroneo@uniparthenope.it; paola.deruggiero@uniparthenope.it; giannetta.fusco@uniparthenope.it

A. Buono · V. Corcione · F. Nunziata
Department of Engineering, University of Naples Parthenope, Naples, Italy
e-mail: andrea.buono@uniparthenope.it; valeria.corcione@uniparthenope.it; ferdinando.nunziata@uniparthenope.it

P. Daponte et al. (eds.), *Measurement for the Sea*, Springer Series in Measurement Science and Technology,
https://doi.org/10.1007/978-3-030-82024-4_8

applications, from ocean color to infrared observations of sea surface temperature, passive microwaves, and altimetry, are addressed. Finally, a special attention is devoted to synthetic aperture radars (SARs) and the emerging role of microsatellites in observing ocean variables and, in particular, wind speed.

8.1 Introduction

During the past five decades, rapid technological growth has advanced the ability of satellites to observe and monitor the global ocean and its overlying atmosphere. Besides several pioneer activities experimented after the invention of photography (e.g., cameras mounted on balloons or pigeons), satellite remote sensing of the ocean began between 1960s and 1970s of the last century, when the USA launched the first meteorological observational satellites [1]. Since that time, many countries have launched satellites that carry instrumentations that allow us to observe several oceanic variables, including sea surface temperature (SST) and salinity (SSS), the concentrations of phytoplankton, sediments and suspended and dissolved material, the changes in sea surface height associated with current systems, the global distribution of ocean waves, the wind speed and direction, the extent of polar sea ice, and many other derived information. In recent years, international agreements among different countries also favored the constellations of smaller satellites that usually focus on a specific ocean feature or phenomenon flying in complementary orbits, so that the coverage by a single satellite is enhanced by observations from the other constellation members. The multi-instrument Envisat mission, equipped with ten instruments operating at both microwave and optical frequencies, for example, has been replaced by the European Space Agency (ESA) Sentinel series of satellites, each one specialized on a different topic.

Prior to satellite oceanography, sea surface properties were determined only from dedicated and expensive ship expeditions, so that the ocean could be surveyed only slowly and incrementally. Earth-orbiting satellite sensors can indeed achieve large-scale synoptic observations that, therefore, enable the monitoring of several oceanic variables at different spatial scales and with a dense temporal sampling. This information is usually provided at short time delays and is used to produce time series several years long. The immediate availability of simultaneous data over large ocean areas is essential for assimilation into numerical models that contribute to weather and climate forecast.

Satellite oceanography is of course limited by a number of issues. Firstly, the penetration depth resulting from the range of frequencies used to collect remotely sensed measurements limits ocean monitoring to surface and near-surface parameters. However, there is limited possibility to get direct information about the underlying water column. Hence, remotely sensed information can be completed by measurements performed by moored and drifting buoys, or by 3D reconstructions inferred through machine learning and statistical techniques applied to satellite observations [2, 3].

Generally, in situ and satellite data should be viewed as an integrated system in order to enhance our knowledge of the physical and biogeochemical characteristics of the four-dimensional ocean. Several studies already demonstrated that the combination of in situ observational networks enhanced spatial and temporal coverage of space-born remote sensing, and numerical simulations booted a number of oceanographic applications to address major concerns like global monitoring, disaster management support, and climate change issues [4]. To ensure that its effect will be pervasive, in science, industry, and social welfare, the satellite oceanography community is working to strengthen the networking among different measurement technologies, provide a more efficient management of the processing chain—from the sensor to the user, improve the assessment of the different available observations and the combination of the different types of measurements (especially for coastal applications), and enhance data management and mining techniques to fully exploit the large amount of available information.

In this chapter, we provide a brief understanding of the rationale that underpins satellite remote sensing—from orbits to generic data processing (Sect. 8.2). Then, an overview of the main satellite oceanography techniques is provided focusing on the main aspects of ocean color (Sect. 8.3), thermal infrared temperature detection (Sect. 8.4), passive microwave radiometry (Sect. 8.5), altimetry (Sect. 8.6), and SAR (Sect. 8.7).

8.2 Technical Background

8.2.1 Electromagnetic Radiation

Ocean remote sensing can be defined as the use of electromagnetic radiation to collect information about the ocean without being in physical contact with the sea surface under investigation [1]. Sea properties are inferred by analyzing the properties (e.g., the intensity and frequency distribution and the polarization) of the electromagnetic radiation received by the satellite-based sensors. This received radiation depends on a number of geophysical variables that—at once—affect the radiation emitted by the ocean, the reflected solar radiation, and the backscattered energy. Remote sensing instruments can be divided into imaging tools (e.g., the SAR, which natively provides measurements arranged as two-dimensional maps that are also known as images) and nonimaging tools (e.g., the microwave radiometer, which provides measurements in a swath-based fashion). The frequency that characterizes the remote sensing instrument must be selected to trade off a number of issues, e.g., capability of penetrating the atmosphere and sensitivity to the geophysical parameter of interest. Accordingly, the bands commonly adopted include visible (VIS), infrared (IR), and microwaves (MW); see Fig. 8.1a. VIS and near-IR (NIR) observations strongly depend on reflected sunlight so that they are restricted to daytime cloud-free periods. IR can be also performed during nighttime, but they are affected

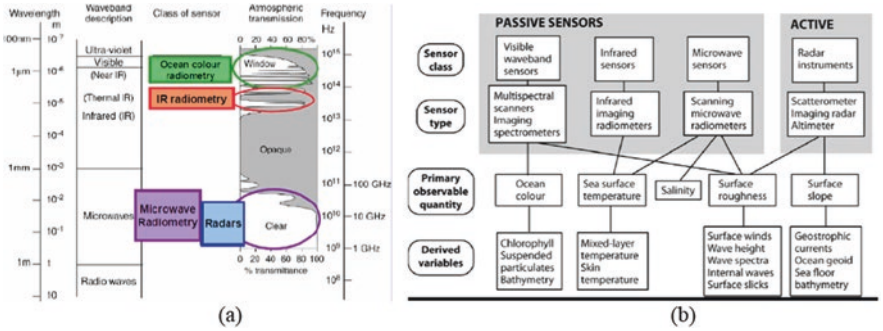

Fig. 8.1 (**a**) Electromagnetic spectrum and the bands used for satellite oceanography according to atmospheric transmission windows; (**b**) an overview of the sensors used for satellite oceanography and the derived ocean variables (adapted from [5])

by clouds. Conversely, the MW part of the spectrum allows all-day and almost all-weather observations. Remote sensing tools can be also divided into passive and active. The passive microwave (PMW) instruments measure the naturally emitted blackbody radiation, while the active sensors transmit bur of signals and receive the electromagnetic wave that—after the interaction with the ocean—reaches the antenna. The latter can be the same antenna used in the transmission phase (monostatic configuration) or an antenna hosted by a different satellite (bistatic configuration or multistatic configuration when multiple antennas are used). Figure 8.1b provides a useful summary of the different remote sensing groups of sensors used in satellite oceanography, along with their applications, as previously reported in [6].

8.2.2 Satellite Orbits

Ocean observation sensors are usually equipped onboard of Earth-orbiting (either geostationary or near-polar) satellites. The geostationary orbit is characterized by a period of one sidereal day (about 23.93 h), being located over the Equator at a height of about 35,800 km to ensure that the satellites always observed a fixed target area on the ground. The sensors onboard of these satellites can observe only part of the Earth that is limited to lower latitudes. Near-polar orbits call for lower altitude (typically 700–1350 km), and they are characterized by an orbital period of about 100 min, so that satellites usually complete 14–15 orbits per day. Since the Earth rotates itself, satellites flying on these orbits cover the ground about 14 times along both descending (northeast–southwest) and ascending (southeast–northwest) tracks. Frequently, low near-polar orbits used for Earth observation are also arranged to be sun-synchronous in order to cross the Equator always at the same local solar time. This is important to boost interoperability among different sensors (e.g., to verify SAR-based wind estimations using nearly timely colocated scatterometer-based winds), to provide daily observations of SST or ocean chlorophyll at the same time

in their diurnal cycle and to minimize cloud cover disturbance through the choice of a specific crossing time. Conversely, according to this orbit, the satellites do not pass directly over the poles reducing the coverage of these regions and giving rise to the famous "hole at the pole." Besides the constraints of the platform on which it is placed, it is important to emphasize that every instrument has its own space-time sampling capabilities which can usually depend on the sensor itself [1].

8.2.3 Imaging Techniques and Data Processing

Remotely sensed satellite products consist of millions of individual measurements collected by a specific sensor over a short length time interval by exploiting a sampling pattern over the observed scene. This scene is referred to as instantaneous field of view (IFOV). Generally, each measured value represents the average of a variable property over the IFOV region observed during a finite time. Some sensors simply make downward-looking observations at periodic intervals, while the satellite moves over the ground, and others scan sideways across the satellite track direction. The former class of sensors provides an average value of the variable in the IFOV that is typically centered at the nadir (i.e., the point on the ground placed immediately below the satellite). The latter gives a wide swath usually centered on the satellite ground track. The scanning and imaging mechanisms are different from sensor to sensor, as fully discussed in [6].

The raw data received by the sensor are converted into scientific units with a proper precision and accuracy which describe an observed geophysical variable. The processing of the swath data includes several steps which are extremely relevant for the interpretation and application of the final ocean products. Thus, the users should be aware of all calibrations, corrections, analyses, and resampling that may have been applied to the satellite data before being released as quantitative information about an ocean variable. The main steps which are generally used to describe the processing tasks can be summarized into four stages of data processing which correspond to different levels of satellite products [7]:

- Level 0—unprocessed raw data acquired by the sensor, in standard binary format;
- Level 1A—Level 0 data processed and converted into an estimate of the electromagnetic property which the sensor is intended to detect, with related ancillary data (e.g., time, calibration coefficients, and geolocation information);
- Level 1B—Level 1A data converted into sensor units (e.g., radiances and brightness temperatures) and organized through along-track swaths;
- Level 2—geophysical products (e.g., SST, SSS, and sea ice cover) in a swath format with same resolution of Level 1 products. They can represent the physical interpretation of the Level 1 units, usually derived from the combination of data from multiple channels and including an atmospheric correction;
- Level 3—geophysical data mapped to uniform grids. Even though averaged in space and time from several Level 2 passes, they may still have gaps associated

with no data due to the swath geometry and/or the cloud cover. The pixel size is usually larger than the native Level 2 one. These products are useful to extend the ocean monitoring beyond the space-time constraints of a single overpass.
– Level 4—Level 3 products combined with information from multiple platforms (e.g., different satellites, in situ measurements, and model outputs) to obtain a gap-free product on uniform grid.

8.3 Visible Imagery

8.3.1 Ocean Color Measurements

Satellite remote sensing of ocean color (OC) is today an indispensable tool for environmental monitoring of the open and coastal ocean. When solar radiation hits the surface of the water, it is absorbed, transmitted, scattered, or reflected by water molecules and by other optically active particles in suspension in the upper layer of the ocean. OC radiometers detect the fraction of sunlight reemitted by the ocean surface after interaction with the water and any suspended matter and allow the retrieval of all the geophysical parameters that can be estimated through the observation of the sea surface at the visible wavelength bands of the electromagnetic spectrum [8].

This signal provides a reliable basis for estimating the concentration of chlorophyll associated with the phytoplankton of the upper ocean, that is, the main contribution of remote sensing to ocean biological science. Phytoplankton are the primary producers of organic matter and the base of the food web in the ocean. They include all the marine algae that absorb light in the blue and red regions of the spectrum and reflect green light, thanks to the presence of chlorophyll pigments. Accordingly, as the concentration of phytoplankton increases in the water, the color of the water (blue) shifts toward the green [5]. For this reason, OC observations are used for monitoring large-scale seasonal and interannual phytoplankton dynamics, analyzing its role in the global carbon cycle, and studying the response of marine ecosystems to climate change [9].

In coastal areas, chlorophyll contribution needs to be distinguished from that of resuspended particulates, colored dissolved organic matter not associated with phytoplankton, and terrestrial suspended particulates due to river runoff. Several specific algorithms permit their identification, proving to be an excellent tool for monitoring coastal eutrophication, algal blooms, sediment plumes, and pollution, as well as their evolution due to coastal currents, storms, and tides, and provide reliable data which can also be assimilated in biogeochemical models [9].

8.3.2 Sensors and Platforms

The OC observations from the space began in the 1970s with the launch of the multichannel scanning radiometer Coastal Zone Color Scanner (CZCS) onboard NASA Nimbus 7 satellite. Since then, several sensors have monitored the global ocean with a spatial and temporal sampling depending on the type of satellite mission and platform. A summary of main OC instruments is reported in Table 8.1.

Given the biological, oceanographic and atmospheric constraints that characterize Earth observation in the visible bands (see Sect. 8.2.1), similar wavelengths, atmospheric corrections, and resolutions characterize the different available instruments [1].

Generally, the operating OC sensors have several spectral bands spanning the visible wavelengths (400–700 nm), which are carefully selected on the specific response of several targets, e.g., the reflectance of open ocean waters and the phytoplankton pigment absorption. Additional bands in the NIR and the short-wave infrared (SWIR) are used indeed to provide atmospheric corrections. Among others, the recent Ocean and Land Color Imager (OLCI) sensor, flown on ESA Copernicus Sentinel-3 satellites since 2016, has even 21 spectral bands from 400 to 1020 nm which measure reflected solar radiation at a ground spatial resolution of about 300 m [10].

Most of the current and defunct sensors were mounted on sun-synchronous polar orbiting satellites (e.g., CZCS, SeaWiFS, VIIRS, and MODIS) and were conceived for having wide sampling swaths in order to provide a global coverage of the Earth surface, at about 0.25–1 km resolution, every 3 days (at the equator) and more frequently at the poles. Nevertheless, to overcome the limitations due to cloud cover, OC data are frequently used as L3/L4 averaged (weekly, monthly, and seasonal) or aggregated (4–9 km pixels) products to obtain continuous and reliable representations of the global ocean and marginal seas.

The observed geophysical parameters usually include chlorophyll concentration, cyanobacterial pigments, total suspended matter, colored dissolved organic matter, diffuse attenuation coefficient, and turbidity. Suitable and potential use from different sensors is reported in Table 8.1.

OC sensors are also mounted on geostationary orbiting satellites, e.g., the Geostationary Ocean Color Imager (GOCI) instrument launched by the Korea Institute of Ocean Science and Technology (KIOST) in June 2010. Thanks to their repeated high-resolution observations over specific regions, these platforms improve the mitigation of the effects of cloud cover and provide biological parameters variability over daily or subdaily temporal scales [11].

Additionally, new requirements from user communities (e.g., a detailed monitoring of coastal and estuarine areas) promoted the development of a new generation of hyperspectral radiometers which are able to sample the full visible spectrum and provide very high-resolution observations for selected areas with more than one sampling per day. In this framework, even though designed for terrestrial applications, the US Geological Survey Landsat 8 OLI sensor and the ESA Copernicus

Table 8.1 A summary of relevant operating OC sensors (adapted from [8]). Potential and suitable geophysical parameters are listed as chlorophyll concentration (Chl), cyanobacterial pigments (CYP), total suspended matter (TSM), colored dissolved organic matter (CDOM), diffuse attenuation coefficient (Kd), and turbidity/Secchi disk depth (Turb/SD)

Type	Platform	Sensor	Pixel size	Spectral bands	Revisit frequency	Launch	Variables					
							Chl	CYP	TSM	CDOM	Kd	Turb/SD
Sun-sync	Terra/Aqua	MODIS	1 km	9	Daily	1999/2000	✓	✓	✓	✓	✓	✓
Sun-sync	Suomi NOAA-20	VIIRS	750 m	7	Daily	2011/2017	✓	✓	✓	✓	✓	✓
Sun-sync	SENTINEL 3 A/B	OLCI	300 m	21	Daily (2 satellites)	2016/2018	✓	✓	✓	✓	✓	✓
GEO	KOMPSAT	GOCI	500 m	8	Half hourly	2010	✓	p	✓	✓	✓	✓
GEO	KOMPSAT-3B	GOCI	500 m	8	Half hourly	2019	✓	p	✓	✓	✓	✓
Sun-sync	Terra/Aqua	MODIS	500 m	2	Daily	1999/2002	p		✓	p	p	p
Sun-sync	LANDSAT 8	OLI	30 m	5	16 days	2013	p	✓	✓	p	✓	✓
Sun-sync	SENTINEL 2	MSI	10–60 m	10	10 days per sensor; 5 days with two S-2	2015	✓	✓	✓	✓	✓	✓

✓ = suitable, p = potential.

Sentinel-2 MSI provide high-resolution (10–60 m) data which allow the monitoring of coastal floating vegetation, suspended particulates, and inland water color, as well as the identification of different types of phytoplankton, including those responsible for harmful algal blooms [8].

8.3.3 Ocean Color Applications

OC remote sensing has many biological applications linked to the estimation of chlorophyll concentration, primary productivity, phytoplankton physiology and distribution, and their linkage at multiple trophic levels of the ocean food web. Marine ecology studies on *Posidonia oceanica* meadows, fish species like anchovies and sardines, which eat phytoplankton in their life cycle, as well as distribution, movement, and migration of various marine species (e.g., whales, dolphins, pinnipeds, penguins, and turtles), have been developed analyzing chlorophyll patterns. OC data also demonstrated that the recruitment success of the fish planktonic larvae, usually transported by ocean currents, is directly related to the degree of timing between spawning and the seasonal phytoplankton blooms. Still, even studies on the distribution of other species as invertebrates, pteropods, pelagic molluscs, and cephalopods have been supported by satellite OC observations [9].

In physical oceanography, OC products are successfully used for the detection and analysis of basin-scale structures and regional dynamics, including eddies, oceanic fronts, and convergence zones in different areas of the global ocean [12, 13]. Since the visible radiation captures better the frontal features than SST data alone, thanks to the effect of dynamical processes on biological life, satellite-derived OC information represents a useful indicator to readily identify the upwelling regions in the oceans. The upwelling processes bring cold, nutrient-rich waters up to the surface, so time series of chlorophyll concentration can easily describe their temporal and spatial variability.

Another OC parameter profitably used in coastal oceanography is the diffuse attenuation coefficient (Kd), which is representative of the total water turbidity and provides valuable information about the dispersion and transport of turbid coastal waters [14].

These applications are extremely useful for several economical and societal activities, such as fishery and aquaculture management, marine protected area monitoring, ecosystem models improvement, and hazard monitoring due to water quality, eutrophication, and harmful algal blooms. In South Africa, for example, the availability of regular OC hyperspectral data assists in discrimination of certain harmful algal species which have previously provided negative impacts on aquaculture and which can be distinguished from spectral features. Along Indian coast, OC data have been proficiently used for location of productive regions through the analysis of oceanographic processes important for enrichment of nutrients (e.g., upwelling and convective mixing) and for creation of maps of potential fishing zones which help to optimize fishery and contrast overfishing [9].

8.4 Infrared Radiometry

8.4.1 Sea Surface Temperature Infrared Observations

IR satellite observations consist of measurements of the blackbody radiation emitted from the top few micrometers of the sea surface. Thus, the retrieved SST should be considered as a measure of the ocean skin temperature. A complete description of thermal skin effects, diurnal variability, and atmospheric corrections can be found in [15].

The first reliable quantitative satellite observations of SST started in 1979 when the first radiometers with multiple IR and MW channels were deployed and allowed corrections for the effects of the atmosphere. From the advanced very high-resolution infrared radiometer (AVHRR) on, satellite measurements provided exceptional information to study global climate change and regional ocean dynamics (e.g., eddies and filaments, upwelling/downwelling, and ocean fronts), and support anthropic sea activities (e.g., fisheries, ship routing, and forecasting). To this aim, since 2002, an important role has been played by the Group for High-Resolution SST (GHRSST) which includes scientists and operational practitioners to discuss issues and results, and coordinate research and operational activities [16]. Besides AVHRR on METOP satellites series and NOAA polar orbiting platforms, at present, IR observations are also collected by MODIS (since 2002) and VIIRS (since 2011) which provide broad swath (2300–3000 km) daily observations at 0.75–1 km resolution, as well as by several instruments flown by India, Japan, and China space agencies and Earth observation centers. A technical and historical description of IR instruments is provided by [15].

Several geosynchronous satellites also collect IR observations, e.g., the Spinning Enhanced Visible and Infrared Imager (SEVIRI) on the Meteosat Second Generation satellite, and the Japanese MTSAT VIS/IR imager and the Advanced Baseline Imager (ABI) on the GOES-R. They all operate with resolutions of 1–4 km and impressive (up to 30 minutes) revisit time [5].

Although information is acquired at different bands of the IR spectrum, MODIS, VIIRS and the geosynchronous instruments use similar algorithms to retrieve SST from pixels which are not affected by clouds or aerosols. Given the strong correlation existing between the atmospheric water vapor content and SST, these algorithms usually involve two bands to remove or minimize the effects of the atmosphere and include different series of diurnal and nighttime empirical regression coefficients (a_n) derived from matchup observations [17]. This split-window technique is implemented as a simple nonlinear combination of measured brightness temperatures [18] having the form of

$$SST\left(^{\circ}C\right) = a_0 + a_1 T_{\lambda_1} + a_2 T_R \left(T_{\lambda_1} - T_{\lambda_2}\right) + a_3 \left(T_{\lambda_1} - T_{\lambda_2}\right)\left(\sec\theta - 1\right) \qquad (8.1)$$

where T_{λ_1} and T_{λ_2} are the temperatures (in K) measured at wavelengths where the atmosphere is relatively transmissive (11–12 μm), T_R is the daily "first-guess" estimate of the SST in the area (in °C), and θ is the satellite zenith angle measured at surface. It is important to emphasize that for nighttime retrievals, observations at mid-IR bands (3.5–4 μm) can also be used for obtaining more accurate products.

The along-track scanning radiometer (ATSR) equipped onboard of the ERS-1/2 and the Advanced ATSR (AATSR) flown on Envisat used an approach different from the split-window technique to remove the atmospheric effect on the observed radiances and, therefore, to obtain reliable SST retrievals at 1 km resolution and about 0.3–0.4 K standard deviation [19]. In fact, those instruments are designed to acquire multichannel information with a dual-look-angle technique [20], that is, observing the same element of ocean surface through two different atmospheric path lengths in an interval of time short enough so that the SST and atmospheric conditions do not change. The dual-look successor to AATSR is the sea and land surface temperature radiometer (SLSTR) that operates in a similar manner on ESA Copernicus Sentinel-3a and Sentinel-3b since 2016 and 2018, respectively. This instrument uses two scan mechanisms and a flip mirror to enable wider swath and takes advantage of an accurate self-calibration of the measured radiances that is achieved using two onboard blackbody cavities [15].

8.4.2 Ice Surface Temperature

Split-window technique has been also adapted to retrieve ice surface temperature (IST) over ice fields that cover the sea surface in polar regions. To this purpose, specific Arctic and Antarctic sets of regression coefficients have been derived in order to consider the unique polar ocean characteristics [21]. An interesting IST application has been devoted to the monitoring of polynyas [22], the recurring and quasi-permanent highly dynamic areas of open water which interrupt the continuous ice cover regulating the exchange of heat, energy, mass, and momentum between the ocean and the atmosphere, and represent important hot spots for ice production, deep-water formation, and ventilation of the global oceans [23].

The polynyas extent variability is probably the most useful variable that can be retrieved from satellite imagery to study these areas. The presence of strong gradients of temperature, associated with the transition between open water and ice field, makes IST information an excellent variable to detect polynyas edges with a good accuracy [24], independently from the exact IST value that is retrieved (Fig. 8.2). Despite the constraints of necessary clear-sky scenes and the better estimations provided by high-resolution SAR imagery [25, 26], the availability of multiple IR observations a day (e.g., from MODIS acquisitions) usually reduces gaps in daily monitoring of several polynya areas [22].

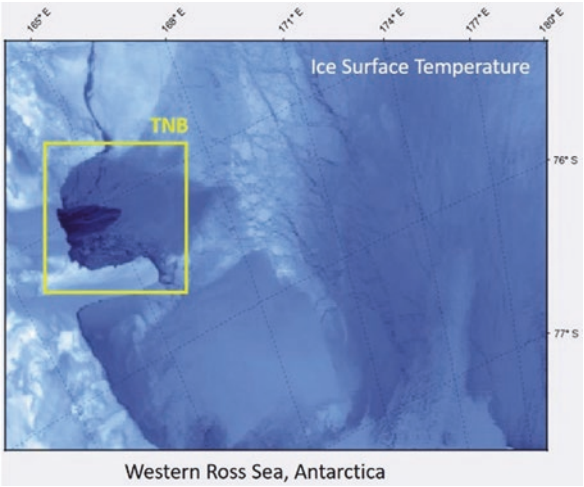

Fig. 8.2 Terra Nova Bay (TNB—yellow square) polynya area (dark blue) observed through MODIS derived ice surface temperature retrievals on September 15, 2014. Estimated polynya extent is about 1428 km^2

8.5 Passive Microwave Radiometry

8.5.1 Physical Aspects

MW radiometers are passive instruments that observe the radiation naturally emitted by the sea surface and that can be used to retrieve several atmospheric and ocean properties, such as SST, SSS, the extent and concentration of sea ice cover, the wind speed, and the rain rate over the ocean. These sensors provide global all-weather coverage, both day and night. Since the atmosphere is much more transparent than in the VIS and IR (VIR), especially in the range between 1 and 10 GHz, MW instruments can view the surface through clouds and gather data under almost all-weather conditions except heavy rain.

At the MW frequencies, the Planck's function can be approximated to the Rayleigh–Jean law [15], so that the emitted radiance varies linearly with the surface physical temperature (T_S) within a frequency interval. As in the IR, the MW brightness temperature (T_B), i.e., the temperature of the black body source that would generate the measured radiance, is related to the physical temperature by the sea surface dielectric properties of the sea surface, which are described by its emissivity (ε), as summarized by the radiative transfer equation [27].

$$T_B = \varepsilon\, t\, T_S + (1-t)\overline{T} + (1-t)(1-\varepsilon)\, t\, \overline{T} + (1-\varepsilon)\, t^2 \left(T_{\text{sun}} + T_{ext}\right) \tag{8.2}$$

where (1–ε) represents reflectivity, t is transmissivity, $\overline{T}$ is the vertical average of the tropospheric temperature profile, T_{sun} is the solar T_B, and T_{ext} is the extraterrestrial brightness temperature exclusive of the sun.

Its approximation in the polar atmosphere

$$T_B\left[\lambda,p\right]=\varepsilon\left[\lambda,p\right]\cdot T_S \tag{8.3}$$

also suggests that T_B is a function of polarization (p). In fact, ocean MW emission is strongly polarized, as it depends on the orientation of the electric field in the plane of incidence with the emitting surface. Since the emissivity changes as the wavelength and polarization vary, the T_B measured at different wavelengths and at different polarizations can be used to retrieve information about the characteristics of the seawater that is emitting the radiation. Considering how each factor differentially affects different MW frequencies, multifrequency and multipolarization radiometers can be used to observe sea surface and retrieve several geophysical parameters by using empirical algorithms, calibrated and validated versus in situ observations. Frequencies used in PMW retrieval of oceanic variables are restricted to specific windows in the range 1–90 GHz to avoid interference from other users, as modern telecommunications and broadcasting infrastructure. These signals would swamp background radiation from natural sources, but by international agreement certain bands are preserved for passive radiometry [5].

Finally, since less energy is available in the MW than in the VIR, a larger aperture or a larger FOV is needed at the long MW wavelengths to obtain the same spatial resolution. Despite significant improvements in swath width, spatial resolution, and spectral diversity have occurred in the last decades, due to size constraints that limit antenna diameters to 1–4 m, at present the resolution of PMW-derived products is usually in the range 3.125–100 km [28].

8.5.2 Wind Speed and Sea Surface Temperature

As mentioned above, the radiation emitted by the sea surface at MW wavelengths depends not only on water temperature and its dielectric properties, but also on the orientation and shape of the sea surface [5]. Consequently, wind speed is one of the parameters that can be retrieved from a multifrequency MW radiometer using empirical algorithms that exploit wind sensitivity at frequencies between 6 GHz and 37 GHz [29]. The first wind speed retrievals date to 1987, thanks to the information collected by the Special Sensor Microwave Imagers (SSM/I) series of instruments carried on the U.S. Defense Meteorological Satellite Program (DMSP). The microwave imager (TMI) on the Japanese–U.S. Tropical Rainfall Measuring Mission (TRMM) satellite and the Japanese Advanced Microwave Scanning Radiometer (AMSR-E) on the NASA Aqua near-polar orbit satellite also provided daily maps of wind speed, since 1997 and 2002, respectively. However, it is important to remark that none of these sensors provide wind direction information as they do for speed (see Chap. 2).

A first fully polarimetric microwave radiometer is indeed the experimental WindSat instrument. It was launched on 2003 onboard the Coriolis spacecraft with

the main purpose of retrieving both speed and direction of the wind from V-pol and H-pol measurements, and provides a cheaper alternative to scatterometers [30].

As for SST, the use of the 6.6 GHz channel, which is sensitive over the full range of sea temperatures, including cold waters, only began in 2002 with the AMSR-E. This sensor provided routine, high-quality, cloud-free, and global mapping of SST over a 1450 km swath, with an accuracy of about 0.4 K and a spatial resolution of about 25 km. Composite daily, weekly, and monthly maps at 1/4°, which are extremely useful to complement infrared radiometers L4 products, are provided as well. In 2012, AMSR-E has been replaced by a second-generation AMSR2 on the Japanese Global Change Observation Mission—Water (GCOM-W) satellite.

SST observations from PMW are also available since 1997 through the TRMM TMI microwave imager but using only the 10.7 GHz channel. Although limited to latitudes lower than 40°, TMI provided continuous observations of the tropical oceans with a resolution of up to 25 km, which allowed the first mapping of mesoscale eddies [31]. As for next-generation satellites, ocean scientists usually suggest SST sensors that could combine the IR and MW channels to provide all-weather SST fields with higher resolution.

8.5.3 Sea Surface Salinity

Sea surface salinity (SSS) is a key component of the water cycle. Its role in ocean density makes it an essential driver of oceanic circulation, a critical parameter for recognizing water masses and understanding their variability and biogeochemical properties, and a tracer of precipitation/evaporation as well as ice melt/freeze.

The retrieval of SSS from microwave radiometry is based on the emissivity of the ocean surface, which depends on the sea surface roughness, and on the dielectric constant of seawater that is a function of temperature and salinity. In such context, three L-band missions, i.e., the ESA Soil Moisture and Ocean Salinity (SMOS) mission [32], the NASA Aquarius mission [33], and Soil Moisture Active Passive (SMAP) observatory [34], provided an unprecedented source of salinity information over the global oceans, which are very useful to improve models and compensate for the scarcity of in situ observations. Since notable differences exist in the instrumental approaches, as well as in the retrieval algorithms and in the dielectric constant models, the three satellite products exhibit SSS errors with a strong dependence on the SST that generally varies with the sensor and version of the products [35].

SMOS satellite was launched in late 2009 and carries aboard an electronically focusing synthetic aperture instrument named MIRAS (Microwave Imaging Radiometer using Aperture Synthesis) operating in L band (1.413 GHz), a protected band at which artificial emissions are forbidden and atmospheric disturbance is negligible. SMOS SSS products are collected over swath of approximately 1000 km with a spatial resolution of 35–50 km and demonstrated good sensitivity of the

ocean surface T_B to SSS in the tropics and subtropics [32]. However, the sensitivity decreases rapidly in cold waters and over areas in which additional undesired effects are due to land–sea and ice–sea contaminations, as well as radio-frequency interference (RFI). Even though L band was supposed to be reserved to science, after the first SMOS data retrievals, the presence of contaminating unlawful sources was indeed noticed [36]. RFI and coast contamination are also challenging in semi-enclosed seas (e.g., the Mediterranean Sea) and represent serious limitations also in Aquarius and SMAP measurements. Nevertheless, several strategies have been developed to overcome these issues and provide new sets of SMOS SSS enhanced data [37, 38]. These enhanced products have been already used, for example, to describe SSS variability at high latitudes [39] or to detect mesoscale structures and reconstruct coherent currents in the Mediterranean Sea [40].

It is important to remark that other than the nominal uses, SMOS has proved to be a versatile satellite, as its data have been used also for additional applications, like wind speed estimation inside tornadoes [41], or the monitoring of the extent and thickness of sea ice [42, 43].

The Aquarius L-band radar/radiometer collected data from August 2011 to June 2015 over a 390 km wide swath with a spatial resolution of about 100–150 km. A complete overview of the progressive improvement obtained in the final version of the released products (i.e., Version 5) and a discussion of the unsolved issues can be found in [44]. Several authors showed that Aquarius data provide reliable information over different areas through comparison with in situ observations and model outputs [45]. Like in SMOS, major issues arise in proximity of coastlines, over areas affected by heavy rain or high RFI and at high latitudes where the L band is less sensitive to SSS. Although the SMAP mission was originally conceived for acquiring direct observations of soil moisture and freeze/thaw, it has been demonstrated that the Aquarius retrieval algorithm can be adapted to retrieve SSS also from this dataset [45].

Future missions are also being planned to enable continuity in the regular and global observation of SSS. Unfortunately, at present SSS products are characterized by a coarse spatial resolution. Next generation of ocean salinity satellite instruments should achieve a much finer spatial resolution (i.e., an order of magnitude) in order to support better the oceanographic, meteorological, and climatological applications [36]. Such improvements cannot be achieved with classical interferometry, so improved techniques should be considered, including the use of a long baseline spatio-temporal interferometer and that of multiple frequencies.

8.5.4 Sea Ice Applications

Sea ice cover has a central role in the albedo feedback mechanisms that regulates climate response at high latitudes and influences the exchange of heat, gases, and momentum between ocean and atmosphere over the polar regions [46, 47]. The monitoring of sea ice extent, concentration, and types represents nowadays a

reliable product of PMW imagers. The dielectric properties of sea ice vary during different stages of growth and decay and are affected by thickness, desalinization, snow cover, roughness, and surface wetness. Thus, the MW emissivity of sea ice is more variable and less predictable than that of seawater, which increases with frequency. The simple formulation of radiative transfer equation in polar regions (Eq. 8.3) and the large differences in open water and sea ice emissivity (T_B contrast is usually >100 K) favored the retrieval of continuous and remarkable ice information on a daily basis. This information allows us to produce composites of the sea ice extent (defined as areas with at least 15% ice coverage) and sea ice concentration variability during the last 40 years and to describe the seasonal to interannual behavior, and the multidecadal trends, in both the Northern and Southern Hemispheres sea ice coverage (Fig. 8.3).

The different responses of the emissivity of open water and sea ice categories to frequency and V/H polarization represent the basis for the algorithms that combine the multifrequency and multipolarization data collected by SSM/I and AMSR-E (and their successors) instruments. SSM/I and SSM/IS (Special Sensor Microwave/Imager Sounder) operate since 1987 (2003) collecting MW observations at 19.35 (V, H), 22.235 (V), 37.0 (V, H), and 85.5 (V, H) GHz. Continuity is available back to 1978, thanks to the scanning multichannel microwave radiometer (SMMR) onboard the NASA NIMBUS-7 spacecraft. Since 2002, AMSR-E (and then AMSR2) employ similar, but not identical, channels at 6.9 (V, H) 10.7 (V, H), 18.7 (V, H), 23.8 (V, H), 36.5 (V, H), and 89.0 (V, H) GHz, with an improved spatial resolution (6.25 km) respect to SSM/I (12.5–25 km). Technical details, issues, and limitations of main empirical algorithms used for sea ice extent and concentration monitoring (e.g., Nasa Team, Bootstrap) are discussed in [48].

Additionally, it is important to remark that first-year ice is saline, while the surface of multiyear ice is nearly fresh and contains many air bubbles (Martin, 2014). Thus, measuring emissivity at different MW frequencies and polarizations also provides valuable information about ice types and thickness as demonstrated in several studies [48–51].

8.6 Synthetic Aperture Radar

8.6.1 Basics of Synthetic Aperture Radar Imaging

SAR is an off-nadir active microwave imaging sensor that allows obtaining fine-resolution images of the Earth's surface day and night under almost any weather conditions latitudes [52]. SAR sensors are usually equipped onboard of aircrafts or satellites in order to exploit the platform's motion to synthesize an antenna longer than its physical dimension. This mechanism makes the spatial resolution of SAR imagery much finer than the one provided by real aperture radars. The image formation process relies on the transmission of modulated microwave pulses while

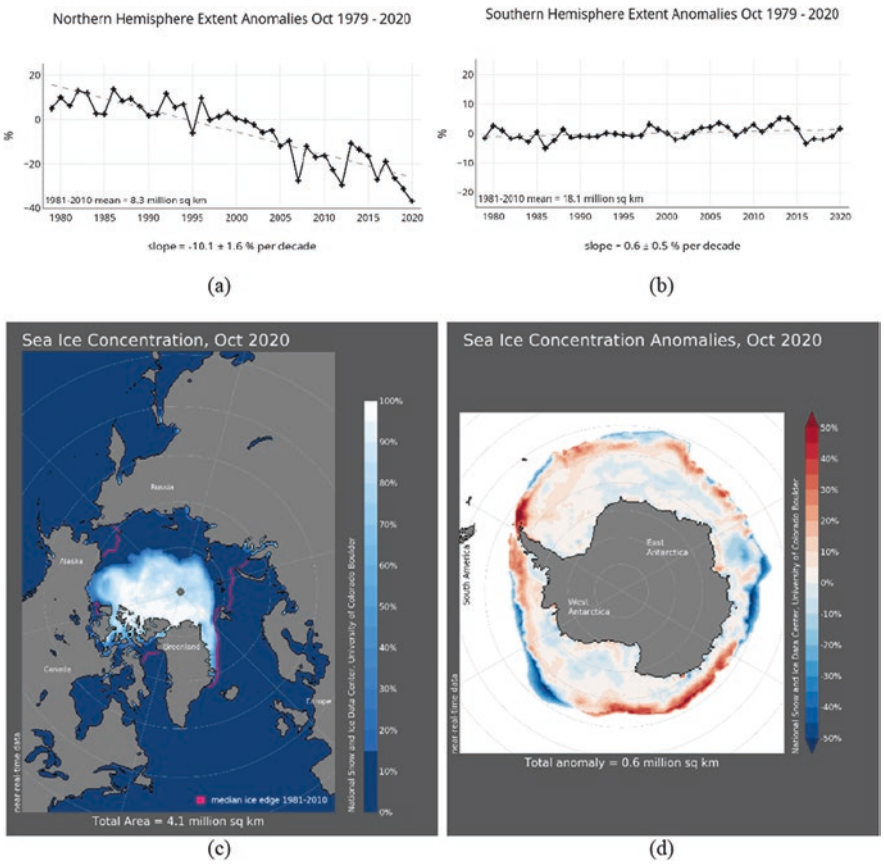

Fig. 8.3 PMW daily and monthly ice extent and concentration products provide a quick look at Arctic- and Antarctic-wide changes in sea ice since 1979. These examples show sea ice extent anomalies during the month of October in the (**a**) Northern and (**b**) Southern Hemisphere since 1979; (**c**) October 2020 sea ice average concentration in the Arctic with an outline of the 30-year (1981–2010) median extent for that month (magenta line); (**d**) October 2020 sea ice concentration anomalies in the Southern Ocean (National Snow and Ice Data Center, University of Boulder Colorado, https://nsidc.org/data/seaice_index)

receiving coherently the echoes scattered off by the observed target. Hence, the SAR image represents a two-dimensional estimation of the target reflectivity which can be linked to the normalized radar cross section (NRCS)—also termed as back-scattering coefficient, σ^0—for each resolution cell [52]. The latter depends on both SAR imaging parameters (wavelength, incidence angle, etc.) and target properties (roughness, moisture, electric permittivity, etc.).

The SAR acquisition geometry is shown in Fig. 8.4. The antenna beam, pointing toward the Earth's surface, illuminates an area termed as footprint, whose width is called swath. The observed area spans two directions: azimuth and range, which are parallel and orthogonal to the platform flight direction, respectively. The ground

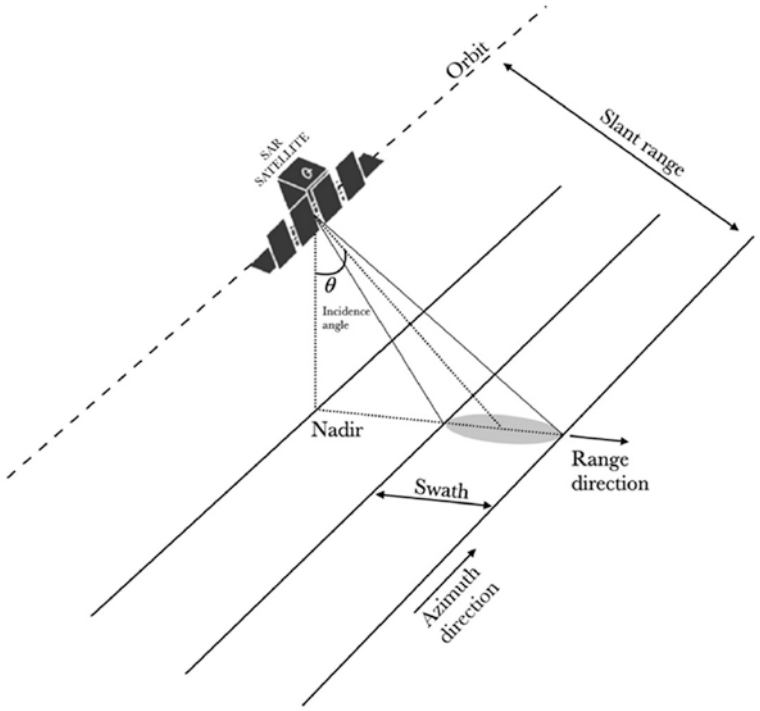

Fig. 8.4 Sketch of the SAR acquisition geometry

area closer to the nadir direction of the SAR sensor is termed near range, while the further one is known as far range. With respect to the nadir, the pointing of the antenna beam defines the incidence angle, which spans from near to far range. When dealing with SAR, the off-nadir looking geometry needed to solve range ambiguities results in a slant range along the line-of-sight direction and a ground range along the Earth's surface, which are related to each other by the incidence angle.

The interpretation of SAR imagery is hampered by the geophysical multiplicative noise that affects any coherent sensor [52]. In fact, the coherent superposition of the backscattered fields due to elementary scatters that lie within each resolution cell results in statistical fluctuations, also known as fading. As a result, gray-tones NRCS SAR images are characterized by a "salt and pepper" appearance termed speckle, which is a random noise that needs to be reduced, at the expenses of the spatial resolution, to improve the capability of extracting reliable information from SAR imagery.

Together with the wavelength of the microwave pulses, an important property that characterizes SAR imaging modes is the polarization. SAR sensors used for Earth observation purposes usually transmit linearly polarized signals, horizontal (H) and/or vertical (V) with reference to the polarization plane, while receiving

coherently in an orthogonal linear H-V basis. The simplest SAR architecture—termed as single-polarization SAR—consists of transmitting a linearly polarized signal while receiving along the same component. When dealing with SAR imaging of the oceans, according to the Bragg/tilted Bragg scattering theory, the vertical polarization is considered to maximize the received signal. Hence, single-polarization SAR operating with a vertical polarization measures the NRCS under vertical transmission and vertical reception, i.e., the VV co-polarized channel σ^0_{VV}. Nevertheless, advanced but more demanding SAR imaging modes, i.e., polarimetric architectures, allow observing the scene under polarization diversity, increasing the geophysical information retrieval capability [53].

The SAR sensors are able to acquire images of the Earth's surface under different imaging modes; each of them is characterized by different spatial resolution, polarization, area coverage, and incidence angle among the various parameters. The most common imaging modes are Stripmap, ScanSAR, and Spotlight [52]. The Stripmap mode consists of illuminating the ground with a continuous sequence of pulse, while the antenna beam is fixed in both azimuth and elevation directions; i.e., a homogeneous scan is made that results in an image quality which is constant along the flight direction. The ScanSAR mode consists of moving the antenna beam along the swath, therefore covering different incidence angles. This results in a reduced azimuth bandwidth and, hence, in a coarser spatial resolution. The Spotlight mode consists of using an observation time as long as the synthetic aperture, resulting in a finer resolution if compared to the Stripmap mode. Spotlight is the finest resolution SAR imaging mode, even if it provides information over a very limited area on the ground.

The main data format for SAR data processing to generate added-value products are single-look complex (SLC) and ground range detected (GRD):

- SLC (Level 1A in Subsect. 8.2.3): SAR images are stored, after raw data focusing, in complex format (real and imaginary part). They are represented in radar coordinates, i.e., over the slant range azimuth plane centered in the zero Doppler point. The product needs radiometric calibration to obtain the NRCS value for each pixel of the image. SLC products are suggested for data processing that needs phase information.
- GRD (Level 1B in Subsect. 8.2.3): SAR images are stored, after raw data focusing, in real format (amplitude). They are represented over the ground range azimuth plane using a reference model for the Earths' ellipsoid. The product needs radiometric calibration to obtain the NRCS value for each pixel of the image. GRD products are suggested for data processing that exploits intensity.

Nowadays, it has been widely demonstrated that SAR satellites represent a key source of information for a broad range of ocean applications including coastline extraction; wind field retrieval; target detection; oil spill monitoring; observation of ocean features as eddies, internal waves, currents; sea ice classification; and extreme weather phenomena observation.

8.6.2 Small-Size Satellites Technology

In very recent years, with the goal of providing a cost-effective and broader access to the space segment even for small companies and universities by trading off satellite planning constraints and launch costs, small-size lighter Earth observation satellites have been launched. This was boosted by the growing developing of engineering technologies in the fields of nano-electronics, micromechanics, solar cells, positioning systems, and telecommunications. In fact, before the beginning of the small satellite era, typical satellite mass was in the range 500 kg–2000 kg, for a cost in the range of 40–170 billion euros, making this market restricted to space agencies and well-established governmental agencies [54]. When dealing with small satellites, mass and cost were dramatically reduced down to few kilograms and few thousand euros, respectively, welcoming into this market many other aerospace operators and private small companies as ICEYE, XpressSAR, and OptiSAR. In addition, the limited costs allow launching experimental space instruments to be tested and validated for research purposes.

Satellites can be grouped according to their mass since it has a direct impact on the launch cost when placed as payload onboard of space vehicles. Small satellites are classified as minisatellites (100–1000 kg), microsatellites (10–100 kg), nanosatellites (1–10 kg), picosatellites (0.1–1 kg), and femtosatellites (0.001–0.1 kg); see Table 8.2.

The fundamental element of most the small-size satellites is the Cubesat, a small-size satellite composed by one or more 10 cm^3 modular units. An "XU" Cubesat indicates a small satellite composed by "X" modular units. The use of Cubesat allows optimizing the hosting capabilities of large launchers; i.e., Cubesat modular units are so small that can be placed as a secondary payload in the extraspace present in large space vehicles in order to put in orbit several small-size satellites with a single launch. Furthermore, the whole Cubesat project from the original idea to the launch takes no longer than 24 months with a total cost that does not exceed 1 billion euros. Several Italian (BlackSky, PlaTino) and international (Quakesat-1, Genesat-1, PRISM, NovaSar, ICEYE) space missions used Cubesat with different payloads depending on the goals of the mission. In 2016, the NRC NASA report found that 34 Cubesat were operating along with 18 space missions, while 46 more

Table 8.2 Satellite classification based on dimension and mass [55]

Satellite class	Mass (kg)
Large	>1000
Mini	100–1000
Micro	10–100
Nano	1–10
Pico	0.1–1
Femto	0.001–0.1

Cubesat were already planned. In 2017, 8 Cubesat missions for Earth observation equipped with optical spectrometers and microwave sensors were developed (three 3 U and five 6 U satellites) by the Earth Science Technology Office (ESTO) under two different NASA space programs: Inflight Validation of Earth Science Technology (InVEST) and Earth Venture Technology [56, 57].

The main planning criteria to be satisfied by the small-size Cubesat satellite can be summarized as follows: minimizing the deployment costs and the risks associated with the instruments; standardizing the modular units; using electronics which is robust to space radiation; and optimizing pointing and propulsion systems. Nowadays, the small-size satellite technology was exploited to host SAR sensors in several space missions. The main mini-SAR satellite (see Table 8.2) missions for Earth observation are as follows [55]:

- NovaSAR-1 (UK, 400 kg);
- TecSAR (Israel, 260 kg);
- SmallSat InSAR (USA/India, 180 kg);
- Micro-XSAR (Japan, 135 kg).

The main micro-SAR satellite (see Table 8.3) missions for Earth observation are as follows:

- ICEYE (Finland, 85 kg);
- Micro-SAR (Norway, 65 kg);
- Capella-XSAR (USA, 48 kg).

8.6.3 The ICEYE Constellation Mission

ICEYE is a Finnish commercial company that was born in 2012 from a research team of the Aalto University. The ICEYE company planned to launch a constellation of 18 sun-synchronous circular orbit (570 km height, 97° inclination)

Table 8.3 Main ICEYE microsatellite characteristics

Satellite characteristic	Value
Carrier frequency (GHz)	9.65, X band
Look direction	Right and left
Antenna size (m)	3.2 × 0.4
Pulse repetition frequency (kHz)	2–10
Range bandwidth (MHz)	10–300
Polarization	VV
Microwave peak power (kW)	4
Total mass (kg)	85

microsatellites in the next few years, offering an unprecedented dense revisit time of 3 h on average, worldwide. Actually, 7 out of the 18 satellites are operating.

The first satellite of the constellation was launched on January 2018 by the Indian rocket PSLV-C40, while the second one was launched in California on December 2018 by the VAFB (Vandenberg Air Force Base) SpaceX Falcon-9 Block 5 launcher, during the SSO-A Spaceflight mission. The last satellite was launched on September 28, 2020, from the Russian Plesetsk Cosmodrome as secondary payload of the Roscosmos Rideshare Soyuz-2.1b/Fregat.

ICEYE satellites are equipped with X-band SAR sensors (carrier frequency around 10 GHz, corresponding to a wavelength of about 3 cm) to keep a small size since the transmitted wavelength is comparable to the actual antenna size [52]. Each SAR belonging to the ICEYE microsatellite constellation is identified by the label "ICEYE-XN," where "N" stands for the satellite identifier. ICEYE-X1 was the first micro-SAR satellite. The main technical features of ICEYE-X2, ICEYE-X4, and ICEYE-X5 are listed in Table 8.4.

It can be noted that they are all equipped with single-polarization VV SAR sensors characterized by a small 3.2 m × 0.4 m phased array antenna, an incidence angle range spanning from 10° to 35° depending on the imaging mode, and total satellite mass of 85 kg. The ICEYE micro-SAR satellites acquire images under two different imaging modes, Stripmap and Spotlight modes, that call for a spatial resolution up to 2.5 m and 0.25 m, respectively. A ScanSAR imaging mode is also planned to be implemented in the near future; see Table 8.3. Note that, independently on the imaging mode, the noise equivalent sigma zero (NESZ), i.e., the noise floor of the SAR instrument, is always better than −19 dB, which is comparable with NESZ values of same imaging modes of conventional X-band SAR satellites as the German TerraSAR-X. As an example, a SAR image collected by ICEYE-X5 over the coast of Port Hedland (Australia) in Stripmap mode is shown, overlapped on the Google Earth map (Fig. 8.5).

Several studies assessed the small-size satellite constellation, including ICEYE, performance with respect to satellite mass, and total cost of the space mission (satellite development and launch); see Fig. 8.6 [54, 58].

Table 8.4 Main features of the ICEYE SAR imaging modes

SAR parameter	Spotlight high	Spotlight	Stripmap high	Stripmap
Area coverage (km^2)	5 × 5	5 × 5	30 × 50	30 × 50
Range × azimuth ground resolution (m)	1 × 1	1 × 1	3 × 3	3 × 3
Range × azimuth slant resolution (m)	0.5 × 0.25	0.5 × 0.5	0.5 × 2.5–3	0.5–1.5 × 2.5–3
NESZ (dB)	≤17	≤17	≤17	≤19
Incidence angle range (°)	20–35	20–35	15–30	15–30

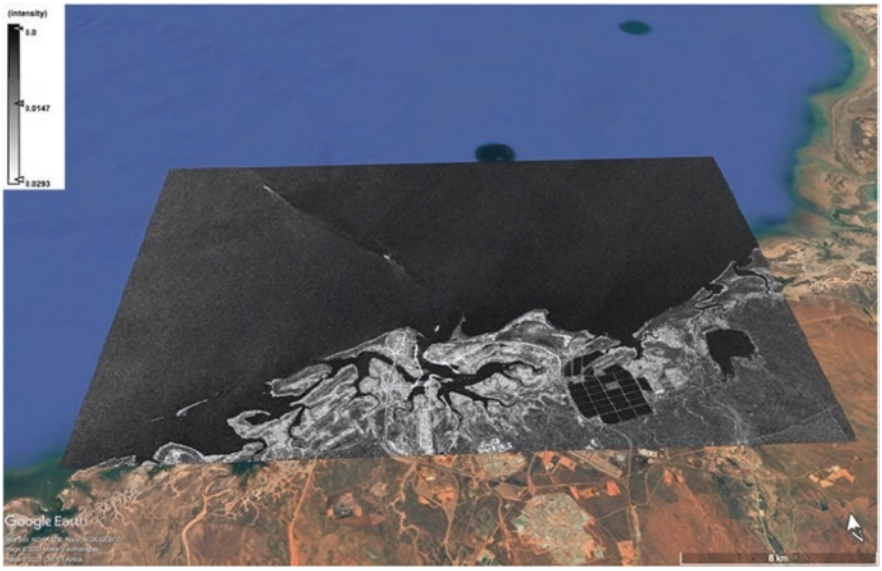

Fig. 8.5 A gray-tones intensity image collected by ICEYE-X5 over the coast of Port Hedland (Australia), superimposed on the Google Earth map

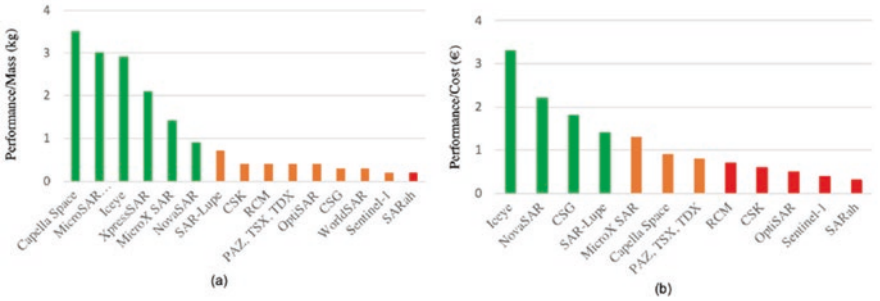

Fig. 8.6 ICEYE performance analysis with respect to (**a**) mass and (**b**) cost [54]

8.6.4 SAR Wind Speed Retrieval

The scattering of the electromagnetic waves from the ocean surface is mainly ruled by the electrical and geometrical properties of the ocean layer involved in the interaction between electromagnetic waves and ocean. At microwave frequencies, the scattering from the wind-roughened ocean surface is the main mechanism. It results from complex nonlinear interactions which are time-dependent and affected by the atmospheric boundary layer [59]. Generally speaking, when the wind blows, short waves that are aligned to the wind direction are generated first, and then, while it continues to blow, large waves are generated until equilibrium is reached. This

reference case, usually assumed in SAR ocean modeling, is known as a fully developed sea [58]. Whenever the fully developed sea case is in question and no swell or coastal effects are present, it is possible to relate the ocean roughness to the local wind speed and direction, i.e., wind field, by a proper modeling, which is at the basis of the scatterometer, i.e., a multibeam real aperture radar that is designed to provide mesoscale estimations of sea surface wind field (see Chap. 2). These sensors offer limited possibility for wind estimation in coastal regions due to land/sea contamination arising from their coarse spatial resolution.

Within this context, the SAR is a key tool to generate high-resolution (up to 1 km) wind maps that are used in local forecasting, typhoon monitoring, and coastal engineering applications. However, unlike the scatterometer, the SAR was not designed for ocean surface wind retrieval, and, therefore, it is impossible to derive both the wind speed and direction based on NRCS values alone. Several approaches have been proposed to deal with wind direction retrieval based on the use of additional wind data sources, e.g., operational meteorological models and wind-aligned features observed in the SAR images (typically in coastal zones) or measurements from other in situ or remote sensors. With respect to wind speed, empirical geophysical model functions (GMFs), originally developed to exploit C-band VV-polarized scatterometer measurements [60, 61], have been tuned and recalibrated to deal with SAR measurements at different frequencies and polarizations. However, when retrieving wind speed using those GMFs, wind direction information must be provided in the retrieval process [60]. This means that errors in the wind direction estimation are propagated into the wind speed estimation.

An alternative approach to the GMF is the so-called azimuth cutoff methodology [62]. It is a spectral method that does not need neither calibration of the data nor any a priori information on wind direction [10] and, therefore, has recently gained more attention [63, 64]. According to [62], the azimuth cutoff λ_c is linked to the directional sea spectrum $S(\omega,\delta,\varphi)$ as follows:

$$\lambda_c = \pi\beta\sqrt{\int_0^\infty \omega^2 S\left(\omega,\delta,\varphi\right) d\omega} \tag{8.4}$$

where ω is the angular frequency of sea waves, δ is the incidence angle, φ is the relative direction of the ω-component of the sea surface spectrum, and β is the ratio between the slant range distance and the velocity of SAR platform.

The retrieval of λ_c from SAR imagery consists of some key steps: (a) The SAR image is partitioned into a number of tails; (b) the autocorrelation function (ACF) is estimated by evaluating the inverse fast Fourier transform (IFFT) of the PSD computed for each tail; (c) speckle noise peaks are mitigated by median filtering; (d) λ_c is estimated as follows [64]:

$$\lambda_c = \sqrt{2\pi\sigma} \tag{8.5}$$

where σ is the standard deviation of the Gaussian bell that best fits the estimated ACF; e) the sea surface wind speed at 10 m above sea level (U) is estimated from the linear relationship [62]:

$$\lambda_c = a + bU \tag{8.6}$$

where a and b are coefficients to be determined from data. Once the azimuth cutoff algorithm was detailed, the sea surface wind speed estimation from ICEYE micro-SAR satellite imagery is showcased to demonstrate the potential of small-size SAR satellites for ocean monitoring. An image collected on September 7, 2019, by the ICEYE-X5 SAR over the coastal area of Port Hedland, northwestern part of Australia, is considered. The fine-resolution image (3 m), covering an area of about 800 km^2, was acquired in VV-polarization Stripmap mode under an incidence angle of 28.5° at midrange.

A multilooked Level 1.1 product with a pixel spacing of 10 m is processed to obtain U on a 1.5 km × 1.5 km grid. The sea surface wind speed map is shown in Fig. 8.7, where the land is masked out in white. It can be observed that low-to-moderate sea state conditions apply over the Port Hedland coastal area at the SAR acquisition time. On average, a wind speed of about 5.45 m/s is estimated. This is consistent with the wind speed information provided by a collocated ASCAT scatterometer product (12.5 km spatial resolution) that results in an average sea surface wind speed of 5.35 m/s.

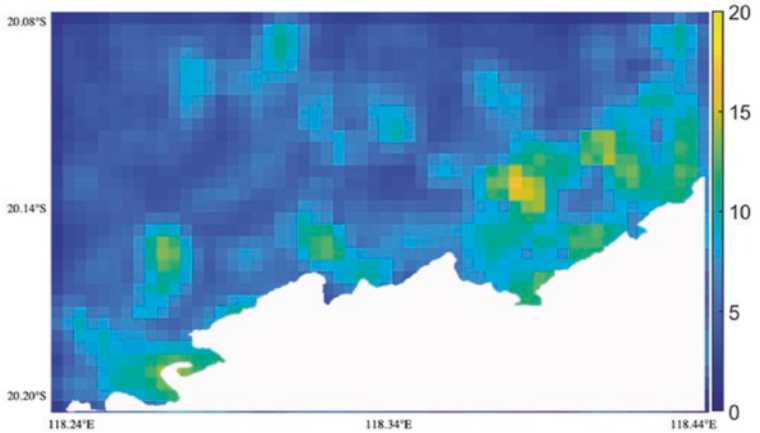

Fig. 8.7 Sea surface wind speed (m/s) map obtained from the ICEYE SAR using the azimuth cutoff approach

8.7 Radar Altimetry

Since 1992 [65], radar altimeters monitor the sea surface topography along the satellite's ground track in order to provide near-global high-precision record of the temporal and spatial scales of ocean variability, the meridional transports of heat, and the distribution and properties of ocean eddies [1]. To this goal, the altimeters transmit short pulses of energy vertically downward toward the surface and then receive the reflected signal. The measure of the time difference between the transmitted and received very short radar pulses gives an estimation of the distance between the satellite and the ocean surface, i.e., of the sea surface height (SSH) associated with tides, geostrophic currents, seafloor topography, and other oceanic phenomena. The shape of the returned electromagnetic signal gives indeed an estimation of the significant wave height (SWH) and the wind speed [31]. Present studies focus on improving resolution and accuracy when approaching the coasts, since the extraction of correct sea level information is still challenging due to corrupted waveforms and imprecise auxiliary information used in the data processing [66, 67]. Additional insights on sea level measurements are provided in Chap. 10.

References

1. Martin S (2014) An introduction to ocean remote sensing, 2nd edn. Cambridge University Press, Cambridge.
2. Sammartino M, Marullo S, Santoleri R, Scardi M (2018) Modelling the vertical distribution of phytoplankton biomass in the Mediterranean Sea from satellite data: a neural network approach. Remote Sens (Basel) 10:1666
3. Nardelli B et al (2020) A deep learning network to retrieve ocean hydrographic profiles from combined satellite and in situ measurements – personal communication. J Geophys Res 12:3151
4. Le Traon PY, Reppucci A, Fanjul EA, Aouf L, Behrens A, Belmonte M et al (2019) From observation to information and users: the Copernicus marine service perspective. Front Mar Sci 6:234
5. Robinson IS (2010) Discovering the ocean from space: the unique applications of satellite oceanography. Springer, Berlin, p 685
6. Robinson IS (2004) Measuring the ocean from space: the principles and methods of satellite oceanography. Springer, Berlin, p 669
7. Parkinson C, Ward A, King M (2006) Earth science reference handbook: a guide to NASA's earth science program and earth observing satellite missions. National Aeronautics and Space Administration, Washington, p 277
8. Groom et al (2019) Satellite Ocean colour: current status and future perspective. Front Mar Sci 6:485
9. Dierssen HM, Radolph K, Lewis E (2013) Remote sensing of ocean colour. In: Orcutt J (ed) Earth system monitoring: selected entries from the encyclopedia 439 of sustainability science and technology. Springer, New York
10. Donlon C, Berruti B, Buongiorno A, Ferreira MH, Femenias P, Frerick J et al (2012) The global monitoring for environment and security (GMES) Sentinel-3 mission. Remote Sens Environ 120:37–57

11. Ruddick K, Neukermans G, Vanhellemont Q, Jolivet D (2014) Challenges and opportunities for geostationary ocean colour remote sensing of regional seas: a review of recent results. Remote Sens Environ 146:63–76
12. Cotroneo Y, Aulicino G, Ruiz S, Pascual A, Budillon G, Fusco G, Tintoré J (2016) Glider and satellite high resolution monitoring of a mesoscale eddy in the algerian basin: effects on the mixed layer depth and biochemistry. J Mar Syst 162:73–88
13. Rivaro P, Ianni C, Langone L, Ori C, Aulicino G, Cotroneo Y, Saggiomo M, Mangoni O (2017) Physical and biological forcing of mesoscale variability in the carbonate system of the Ross Sea (Antarctica) during summer 2014. J Mar Syst 166:144–158
14. de Ruggiero P, Napolitano E, Iacono R, Pierini S (2016) A high-resolution modelling study of the circulation along the Campania coastal system, with a special focus on the Gulf of Naples. Cont Shelf Res 122:85–101
15. Minnett PJ et al (2019) Half a century of satellite remote sensing of sea-surface temperature. Remote Sens Environ 2019:233
16. Donlon CJ et al (2007) The global ocean data assimilation experiment high-Resolution Sea surface temperature pilot project. Bull Am Meteorol Soc 88:1197–1213
17. Kilpatrick KA, Podestá G, Walsh S, Williams E, Halliwell V, Szczodrak M, Brown OB, Minnett PJ, Evans R (2015) A decade of sea surface temperature from MODIS. Remote Sens Environ 165:27–41
18. Walton CC, Pichel WG, Sapper JF, May DA (1998) The development and operational application of nonlinear algorithms for the measurement of sea surface temperatures with the NOAA polar-orbiting environmental satellites. J Geophys Res 103(27):999–928,012
19. Berry D, Corlett G, Embury O, Merchant C (2018) Stability assessment of the (a)ATSR Sea surface temperature climate dataset from the European Space Agency climate change initiative. Remote Sens (Basel) 10:126
20. Llewellyn-Jones DT, Minnett PJ, Saunders RW, Zavody AM (1984) Satellite multichannel infrared measurements of sea surface temperature of the N.E. Atlantic Ocean using AVHRR/2. Q.J.R. Meteorol Soc 110:613–631
21. Hall DK, Key JR, Casey KA, Riggs GA, Cavalieri DJ (2004) Sea-ice surface temperature product from MODIS. IEEE Trans Geosci Remote Sens 42:1076–1087
22. Preußer A, Willmes S, Heinemann G, Paul S (2015) Thin ice dynamics and ice production in the Storfjorden polynya for winter seasons 2002/2003–2013/2014 using MODIS thermal infrared imagery. Cryosphere 9:1063–1073
23. Aulicino G, Sansiviero M, Paul S, Cesarano C, Fusco G, Wadhams P, Budillon G (2018a) A new approach for monitoring the Terra Nova Bay polynya through MODIS ice surface temperature imagery and its validation during 2010 and 2011 winter seasons. Remote Sens (Basel) 10:366
24. Sansiviero M, Morales Maqueda MÁ, Fusco G, Aulicino G, Flocco D, Budillon G (2017) Modelling Sea ice formation in the Terra Nova Bay polynya. J Mar Syst 166:4–25
25. Parmiggiani F (2006) Fluctuations of Terra Nova Bay polynya as observed by active (ASAR) and passive (AMSR-E) microwave radiometers. Int J Remote Sens 27:2459–2467
26. Aulicino G, Wadhams P, Parmiggiani F (2019a) SAR pancake ice thickness retrieval in the terra nova bay (Antarctica) during the PIPERS expedition in winter 2017. Remote Sens (Basel) 11:2510
27. Stewart RH (1985) Methods of satellite oceanography. University of California Press, Berkeley
28. Brodzik MJ, Long DG, Hardman MA, Paget A, Armstrong R (2018) MEaSUREs calibrated enhanced-resolution passive microwave daily EASE-grid 2.0 brightness temperature ESDR, version 1. NASA National Snow and Ice Data Center Distributed Active Archive Center, Boulder
29. Wentz FJ (1997) A well calibrated ocean algorithm for special sensor microwave/imager. J Geophys Res 102:8703–8718
30. Ricciardulli L, Wentz FJ (2015) Ascatterometer geophysical model function for climate-quality winds: QuikSCAT Ku-2011. J Atmos Oceanic Tech 32:1829–1846

31. Fu LL, Lee T, Liu WT, Kwok R (2019) 50 years of satellite remote sensing of the ocean. Meteorol Monogr 59:1–46
32. Mecklenburg S et al (2012) ESA's soil moisture and ocean salinity Mission: Mission performance and operations. IEEE Trans Geosci Remote Sens 50:1354–1366
33. Le Vine DM, Lagerloef GSE, Colomb FR et al (2007) Aquarius: an instrument to monitor sea surface salinity from space. IEEE Trans Geosci Remote Sens 45:2040–2050
34. Entekhabi D et al (2010) The soil moisture active passive (SMAP) mission. Proc IEEE 98:704–716
35. Soldo Y, Cabot F, Rougé B, Kerr YH, Al Bitar A, Epaillard E (2013) SMOS-NEXT: a new concept for soil moisture retrieval from passive interferometric observations. Eur Astron Soc Publ Ser 59:203–212
36. Alvera-Azcarate A, Barth A, Parard G, Beckers J-M (2016) Analysis of SMOS Sea surface salinity data using DINEOF. Remote Sens Environ 180:137–145
37. Olmedo E, Martínez J, Turiel A, Ballabrera-Poy J, Portabella M (2017) Debiased non-Bayesian retrieval: a novel approach to SMOS Sea surface salinity. Remote Sens Environ 193:103–126
38. Olmedo E, Taupier-Letage I, Turiel A, Alvera-Azcaràte A (2018) Improving SMOS Sea surface salinity in the Western Mediterranean Sea through multivariate and multifractal analysis. Remote Sens (Basel) 10:485
39. Aulicino G, Cotroneo Y, Olmedo E, Cesarano C, Fusco G, Budillon G (2019b) In situ and Satellite Sea surface salinity in the Algerian Basin observed through ABACUS glider measurements and BEC SMOS regional products. Remote Sens (Basel) 11:1361
40. Grodsky SA, Reul N, Lagerloef G, Reverdin G, Carton JA, Chapron B, Quilfen Y, Kudryavtsev VN, Kao H-Y (2012) Haline hurricane wake in the Amazon/Orinoco plume: AQUARIUS/SACD and SMOS observation. Geophys Res Lett 39:L20603
41. Kaleschke L, Tian-Kunze X, Maaß N, Mäkynen M, Drusch M (2012) Sea ice thickness retrieval from SMOS brightness temperatures during the Arctic freeze-up period. Geophys Res Lett 39:L05501
42. Mäkynen M et al (2020) Satellite observations for detecting and forecasting sea-ice conditions: a summary of advances made in the SPICES project by the EU's horizon 2020 programme. Remote Sens (Basel) 12:1214
43. Le Vine DM, Dinnat EP, Meissner T, Wentz FJ, Kao HY, Lagerloef G, Lee T (2018) Status of Aquarius and salinity continuity. Remote Sens (Basel) 10:1585
44. Meissner T, Wentz FJ, Le Vine DM (2018) The salinity retrieval algorithms for the NASA Aquarius version 5 and SMAP version 3 releases. Remote Sens (Basel) 10:1121
45. Dinnat EP, Le Vine DM, Boutin J, Meissner T, Lagerloef G (2019) Remote sensing of sea surface salinity: comparison of satellite and in situ observations and impact of retrieval parameters. Remote Sens (Basel) 11:750
46. Cerrone D, Fusco G, Simmonds I, Aulicino G, Budillon G (2017) Dominant covarying climate signals in the southern ocean and antarctic sea ice influence during the last three decades. J Climate 30:3055–3072
47. Wadhams P, Aulicino G, Parmiggiani F, Persson POG, Holt B (2018) Pancake ice thickness mapping in the Beaufort Sea from wave dispersion observed in SAR imagery. J Geophys Res Oceans 123:2213–2237
48. Tateyama K, Enomoto H, Toyota T, Uto S (2002) Sea ice thickness estimated from passive microwave radiometers. Polar Meteorol Glaciol 16:15–31
49. Martin S, Drucker R, Kwok R, Holt B (2004) Estimation of the thin ice thickness and heat fluxes for the Chukchi Sea Alaskan coast polynya from SSM/I data, 1990–2001. J Geophys Res 109:C10012-1–C10012-15
50. Naoki K, Ukita J, Nishio F, Nakayama M, Comiso JC, Gasiewski AJ (2008) Thin sea ice thickness as inferred from passive microwave and in situ observations. J Geophys Res 113:C02S16-1–C02S16-11

51. Aulicino G, Fusco G, Kern S, Budillon G (2014) Estimation of sea-ice thickness in Ross and Weddell seas from SSM/I brightness temperatures. IEEE Trans Geosci Remote Sens 52:4122–4140
52. Richards JA (2009) Remote sensing with imaging radar. Signals and communication technology series. Springer, Berlin
53. Lee JS, Pottier E (2009) Polarimetric radar imaging: from basics to applications. CRC Press, Boca Raton
54. Filippazzo G, Dinand S (2017) The potential impact of small satellite radar constellations on traditional space systems. In: 5th federated and fractionated satellite systems workshop, Toulouse
55. Kramer HJ, Cracknell AP (2008) An overview of small satellites in remote sensing. Int J Remote Sens 29(15):4285–4337
56. Peral E et al (2018) Radar technologies for Earth remote sensing from CubeSat platforms. Proc IEEE 106(3):404–418
57. Paek SW, Balasubramanian S, Kim S, de Weck O (2020) Small-satellite synthetic aperture radar for continuous global Biospheric monitoring: a review. Remote Sens (Basel) 12:2546
58. Deepak RA, Twiggs RJ (2012) Thinking out of the box: space science beyond the CubeSat. J Small Satell 1:3–7
59. Apel JR (1987) Principles of ocean physics, vol 38. Academic, New York
60. Wackerman CC et al (1996) Wind vector retrieval using ERS-1 synthetic aperture radar imagery. IEEE Trans Geosci Remote Sens 34(6):1343–1352
61. Grieco G, Nirchio F, Migliaccio M (2015) Application of state-of-the- art SAR X-band geophysical model functions (GMFs) for sea surface wind (SSW) speed retrieval to a data set of the Italian satellite mission COSMO-SkyMed. Int J Remote Sens 36(9):2296–2312
62. Kerbaol V, Chapron B, Vachon PW (1998) Analysis of ERS-1/2 synthetic aperture radar wave mode images. J Geophys Res Ocean 103(C4):7833–7846
63. Grieco G, Lin W, Migliaccio M, Nirchio F, Portabella M (2016) Dependency of the Sentinel-1 azimuth wavelength cut-off on significant wave height and wind speed. Int J Remote Sens 37(21):5086–5104
64. Corcione V, Grieco G, Portabella M, Nunziata F, Migliaccio M (2019) A novel azimuth cutoff implementation to Retrieve Sea surface wind speed from SAR imagery. IEEE Trans Geosci Remote Sens 57(6):3331–3340
65. Abdallah S et al (2021) Altimetry for the future: building on 25 years of progress. Advances on space research 68(2):319–363.
66. Aulicino G, Cotroneo Y, Ruiz S, Román AS, Pascual A, Fusco G, Tintoré J, Budillon G (2018b) Monitoring the Algerian Basin through glider observations, satellite altimetry and numerical simulations along a SARAL/AltiKa track. J Mar Syst 179:55–71
67. Taburet G, Sanchez-Roman A, Ballarotta M, Pujol M-I, Legeais J-F, Fournier F et al (2019) Duacs dt-2018: 25 years of reprocessed sea level altimeter products. Ocean Sci Discuss 2019:1–30